Available online at www.sciencedirect.com
ScienceDirect
Journal of the European Ceramic Society 27 (2007) 3339–3344
www.elsevier.com/locate/jeurceramsoc

Mechanical properties of alumina-rich magnesium aluminate spinel/tungsten composites

T. Rodriguez-Suarez, S. Lopez-Esteban, J.F. Bartolomé, J.S. Moya *

Instituto de Ciencia de Materiales de Madrid (ICMM), Consejo Superior de Investigaciones Científicas (CSIC), Cantoblanco, 28049 Madrid, Spain

Available online 20 April 2007

Abstract

The mechanical properties and microstructure of alumina-rich magnesium aluminate spinel/tungsten (14 and 22 vol.% W) composites obtained by hot press at 1650 °C under reducing conditions have been investigated. The *R*-curve for these composites was estimated by the indentation strength method and compared with that of the monolithic spinel obtained under similar conditions. Rising *R*-curve behavior was specially observed in the composites when tungsten content was higher. Other mechanical properties such as hardness, toughness, Young's modulus and bending strength, were also determined for both (composites and monolithic magnesium aluminate). Higher values of bending strength were found as the metal volume fraction increases in the composite. The metal content dependence of Young's modulus and Vickers hardness follow the rule of mixtures. Mechanical properties and specially toughness are influenced by the metal content and its grain size.

Keywords: Hot pressing; Composites; Mechanical properties; Strength; *R*-curve

1. Introduction

In the last decades many efforts have been made to improve the mechanical properties of ceramic materials. Brittle ceramics can be toughened by incorporating metallic inclusions into them; hence ceramic/metal composites are very interesting under physical, electrical, optical and mechanical points of view. In this way, it is easy to find many works reported using various metals with different ceramic matrices.[1–4]

Magnesium aluminate spinels have well known optical applications in fabricating vis–UV transparent domes, windows and lamp envelopes,[5–7] and also other structural as for example as catalyst support,[8,9] for nuclear waste management applications,[10] armor,[11] humidity sensors[12] and cement castables.[13] On the other hand, the high melting point of tungsten makes it an obvious choice for structural applications exposed to very high temperatures. Tungsten is used at lower temperatures for applications that can use its high elastic modulus ($E = 411$ GPa), density and considerably high Vickers' hardness ($H_v = 3.43$ GPa). The combination of both components makes the spinel/tungsten composite a promising new material with great technological interest for high temperature applications as could be thermal barriers, ceramic–metal interconectors[14] and also for armor. Ceramics and ceramic/metal composites are emerging in military systems,[15,16] which make use of the low manufacturing cost, light weight, scale-up potential, and unique properties.

The most important factor that made us choose tungsten for our purpose was that the mismatch between the thermal expansion coefficients is low ($\alpha = 5.4 \times 10^{-6}\ K^{-1}$ for the spinel and $\alpha = 4.5 \times 10^{-6}\ K^{-1}$ in the case of tungsten) making this system a model to study. This is a key factor in selecting suitable reinforcement materials in addition to the chemical compatibility with the matrix. Furthermore, both present a refractory character ($T_m = 2135$ °C for this particular spinel and $T_m = 3422$ °C in the case of tungsten). The alumina-based systems are very important to study because this is one of the most common compounds in refractory materials.

This particular system is original and has never been studied before hence the results obtained can be compared with those of other cermets reported in the literature.

The way of processing chosen was the conventional wet route normally followed in other ceramic/metal composites as for example mullite/molybdenum,[17] zirconia/stainless-steel[18] and zirconia/nickel.[19]

The aim of this work was improving spinel brittleness by the inclusion of metallic particles.

* Corresponding author. Tel.: +34 913349083; fax: +34 913349083.
E-mail address: jsmoya@icmm.csic.es (J.S. Moya).

0955-2219/$ – see front matter © 2007 Elsevier Ltd. All rights reserved.
doi:10.1016/j.jeurceramsoc.2007.02.192

2. Experimental procedure

2.1. Starting materials

The following commercially available powders have been used: (1) 99.95% pure W metal (Goodfellow Cambridge, Ltd., UK), with an average particle size <1 μm; (2) Alumina-Rich Magnesium Aluminate Spinel AR78 (Alcoa Industrial Chemicals, Germany) with an average particle size of 4.5 μm and chemical analysis (wt.%): Al_2O_3 (77.1); MgO (22.52); SiO_2 (0.05); Fe_2O_3 (0.08); CaO (0.25).

2.2. Processing of spinel–tungsten composites

Alumina-rich magnesium aluminate spinel commercial powder was first attrition milled in distilled water media with zirconia balls for 3 h until an average particle size of ≈2 μm was reached. After milling, spinel powders were ground in an agate mortar, calcined at 600 °C in air for 1 h in order to burn all organic residues and subsequently passed through a 100 μm sieve. Two different spinel–tungsten suspensions were prepared by mixing milled spinel powder with 14 and 22 vol.% of W, using distilled water as a liquid medium. From now on the samples will be denoted as AR78-14W and AR78-22W, respectively (AR78 is the spinel commercial name and stands for alumina-rich 78%). The solids loading was fixed to 75 wt.% and an anionic polyelectrolyte (Dolapix PC-33) was added (1 wt.% referred to total solids loading) as deflocculant. The mixtures were homogenized by milling with zirconia balls in polyethylene containers at 100 rpm for 24 h and then dried at 90 °C for 24 h. The resulting powders were crushed in an agate mortar. Then the powders were hot-pressed in a carbon die of 50 mm diameter using an Argon atmosphere at 1650 °C and 46 MPa for 1 h avoiding contact with oxygen. Disks of 50 mm in diameter and 8 mm in height were obtained. In terms of comparison, a similar experimental procedure was used to obtain a pure spinel sintered disk.

2.3. Characterization

X-ray diffraction analysis (XRD) of the powders was performed using Cu Kα radiation for phase identification (Bruker D8 diffractometer).

The microstructures of fired specimens were studied on diamond polished surfaces down to 1 μm by scanning electron microscopy (Hitachi, Model S3000N).

Bulk densities for all materials were measured using the Archimedes method, with water as the immersion media.

2.4. Mechanical properties

The hot-pressed disks were machined to obtain prismatic bars with dimensions of 43 mm × 2 mm × 4 mm for measure the mechanical properties. The tensile surface was polished down to 1 μm. Indentation strength tests were performed using prismatic bars in which the centers of the tensile faces were indented with a Vickers diamond indenter (Leco 100-A, St. Joseph, MI) at contact loads, P, between 10 and 500 N. The mechanical test was performed immediately after indentation to avoid any subcritical crack growth due to stress corrosion effects. The specimens were tested at room temperature using a three-point support with a span of 40 mm in a universal testing machine (Instron Model 4411). The specimens were loaded to failure with a crosshead speed of 0.005 cm/min. The bending strength, σ_f, was determined by three-point bending test. Bars were evaluated with a loading direction normal to the hot-pressing direction.

Special effort was made to ensure that in all specimens the indentation contact site acted as the origin of failure; that was verified after testing using a reflected light optical microscopy (Leica, Model DMR).

The hardness was estimated by the Vickers indentation. Young's modulus was obtained from the slopes of load–deflection curves. A static extensometer was used to measure the deflection with an error in the measurement of ≈0.05%.

R-curves (toughness curves) were measured via the indentation-strength method reported by Braun et al.,[20] where a radial crack c is considered to be produced by indentation at a load P and subjected to the action of a tensile stress σ_a due to the applied stress load during three-point bending. During post-indentation bending, the crack is subjected to a total stress intensity, K_t, which is the sum of contributions from the residual stress intensity factor acting on the indentation crack resulting from the elastic-plastic mismatch associated with the indentation, K_r, and the stress intensity factor resulting from the applied stress, K_a:

$$K_t(c) = K_a(c) + K_r(c) = \psi\sigma_a c^{1/2} + \xi\left(\frac{E}{H}\right)^{1/2}\left(\frac{P}{c^{3/2}}\right) = K_R(c) \quad (1)$$

where ψ is a crack geometry factor; ξ a dimensionless geometrical constant; E Young's modulus; H hardness; K_R is the toughness of the material. For a given indentation load, P, failure is assumed to occur at the stress where the applied stress σ_a is equal to the fracture stress, σ_f, which satisfies the following balance and tangency conditions:

$$K_t(c) = K_R(c) \quad (2)$$

$$\frac{dK_t(c)}{dc} = \frac{dK_R(c)}{dc} \quad (3)$$

The *R*-curve is determined by solving Eqs. (2) and (3) for each beam simultaneously. In other words, the *R*-curve is determined as the common envelope of the tangency points to the family of $K_t(c)$ curves from the σ_f (P) data sets.

3. Results and discussion

3.1. Microstructural analysis

The relative densities of the obtained sintered spinel/tungsten composites were found to be >98% of theoretical.

Fig. 1 shows scanning micrographs of the microstructures of different spinel/tungsten composites. Darker and bright phases are spinel and tungsten grains, respectively. The tungsten particles are uniformly dispersed in the matrix and no significant

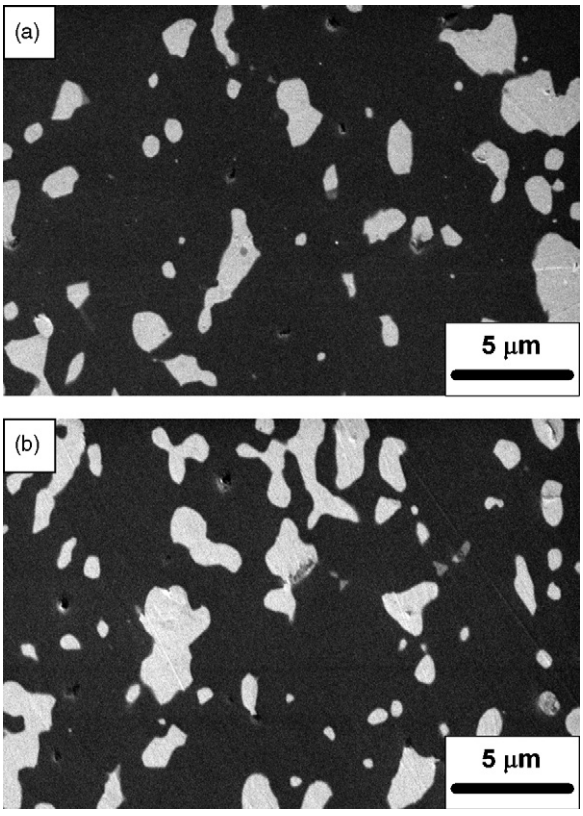

Fig. 1. SEM micrographs of both spinel/tungsten composites: (a) 14 vol.% W and (b) 22 vol.% W.

porosity is observed, in agreement with the density measurements. There is a difference in tungsten grain size and its distribution in both composites. In the AR78-14W composite, a bigger amount of small and rounded W grains are observed while the irregular shapes in larger tungsten particles are less common than in the AR78-22W composite. These larger tungsten particles are the responsible for bridging the cracks thus the toughness in both composites will be different. Round and small tungsten grains are also present in the 22 vol.% W composite but in a less significant amount. It is important to note that no entities of tungsten oxides are detected by EDX analysis, as can be expected after sintering under reducing atmosphere. Ceramic/metal interface is well bonded and no microcracks are observed. Under the same sintering conditions, the matrix grain size of the spinel/tungsten composites is smaller than that of monolithic spinel. This suggests that the presence of W inhibits the grain growth of the matrix. It can be concluded that monolithic spinel (AR78) has a $d_{50} \approx 4.8\,\mu m$; while, for both composites, spinel has a d_{50} of $\approx 3.3\,\mu m$ for the 14 vol.% W content and 3.5 μm for the 22 vol.% W content.

3.2. Mechanical properties

The hardness, Young's modulus and bending strength for the composites and the monolithic spinel are given in Table 1.

Hardness, in the case of all composites, decreases as expected following the rule of mixtures and taking into account tungsten hardness is 3.43 GPa. The same tendency is observed in the case of Young's modulus, values were found to be very close to those predicted by the rule of mixtures.

Table 1
Mean hardness, Young's modulus and bending strength of monolithic spinel and spinel/tungsten composites

Material	Hardness (GPa)	Young modulus (GPa)	Bending strength (MPa)
AR78	14.7 ± 0.5	235 ± 9	264 ± 18
AR78-14W	13.6 ± 0.2	251 ± 16	302 ± 27
AR78-22W	12.3 ± 0.2	263 ± 4	344 ± 19

The fracture strength of the unindented spinel/tungsten composites increased with the metal content of the composites up to ≈30%. This fact can be explained by an increase in toughness, similar critical defect and low residual stress due to a not significant thermal expansion coefficients mismatch.

3.3. Indentation strength R-curves

The fracture strength as a function of the indentation load for monolithic spinel and spinel/tungsten composites is shown in Fig. 2. In terms of comparison, a constant toughness material strength response corresponding to a $P^{-1/3}$ asymptote is also plotted. The strengths for natural flaws of different compositions were arbitrarily plotted at $P = 1$ N. Great care was taken to ensure that the indentation site was the source of the critical flaw for all reported data.

Linear regression was used to obtain the best fit to the data from monolithic spinel and spinel/tungsten composites. It showed that the slopes of monolithic spinel (AR78) and spinel/tungsten composites (AR78-14W and AR78-22W) were 0.27, 0.24 and 0.22, respectively. Griffith materials, which show no rising *R*-curve behavior, present a slope of 1/3, and slopes for *R*-curve materials are lower. Because the slopes of spinel/tungsten composites are less than 1/3, rising *R*-curve behavior is expected. The AR78-22W composite, have higher indentation strength and flaw tolerance than the other composite and monolithic spinel.

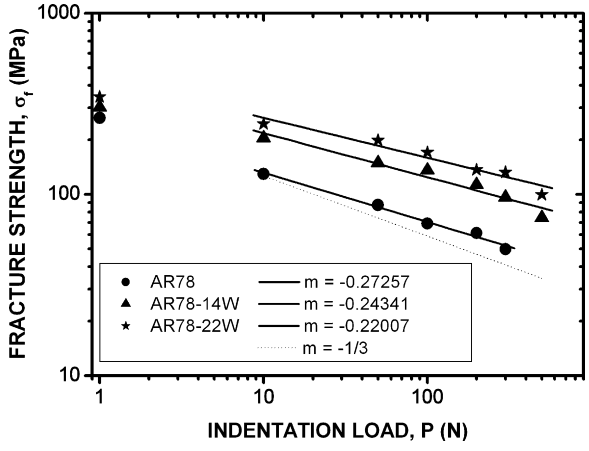

Fig. 2. Fracture strength vs. indentation load plots of spinel and spinel/tungsten composites. The indentation-strength data to the $P^{-1/3}$ strength response is shown by the dashed line.

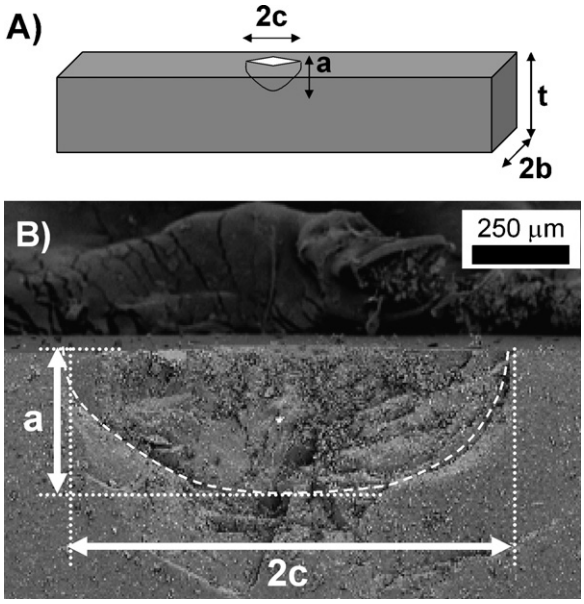

Fig. 3. (A) Indentation scheme made on the prismatic bar and (B) SEM micrograph of the fracture caused by a 500 N load indentation.

This σ_f versus P measurements were subsequently used to deconvolute the R-curve, in accordance with an indentation strength k-field analysis of Braun et al.[20] described above. For the present study, the value of ψ was taken to be ≈1.1.[21] There are no previous works where this value for the magnesium aluminate spinel is reported, but can be estimated when the geometry of the indentation transversal section is known. Fig. 3 shows an indented bar scheme and a scanning picture of the 500 N transversal section indentation without any posterior load applied after its generation. Taking into account that a/c is ≈0.6 and a/t is 0.2, ψ ranges from 0.916 to 1.110 as well as the indentation angle increases (higher indentation loads result in deeper angles). Hence, a mean ψ value of 1.1 is good enough for all calculations with negligible error.

The toughness is plotted as a function of crack length for each (P, σ_f) pair for the monolithic spinel and spinel/tungsten composites in Fig. 4. The value of the geometrical constant $\xi = 0.016$, calibrated by Anstis et al.[22] from a number of brittle materials with known values, and appropriate E and H values from Table 1, were used to generate these plots. The locus of points defining the R-curve were generated with the following relationship developed by Hsueh and Becher[23]

$$C_f = \left[\frac{\xi(E/H)^{1/2}}{\psi}\right]^{1/2} \left(\frac{d\sigma_f}{dP}\right)^{-1/2} \quad (4)$$

where $d\sigma_f/dP$ was found from Fig. 2.

Fig. 5 compares the R-curves of the spinel/tungsten composites with the monolithic spinel. In the case of AR78-22W, the initial toughness is ≈3.5 MPa m$^{1/2}$ and rises to a maximum value of 5.6 MPa m$^{1/2}$. A clear rising R-curve behavior due to the crack wake zone associated to a bridging mechanism is observed. In the case of AR78-14W, the initial toughness is ≈3 MPa m$^{1/2}$ and reaches a maximum value of 4 MPa m$^{1/2}$, a slight R-curve behavior is noted in this composite and a saturated value in

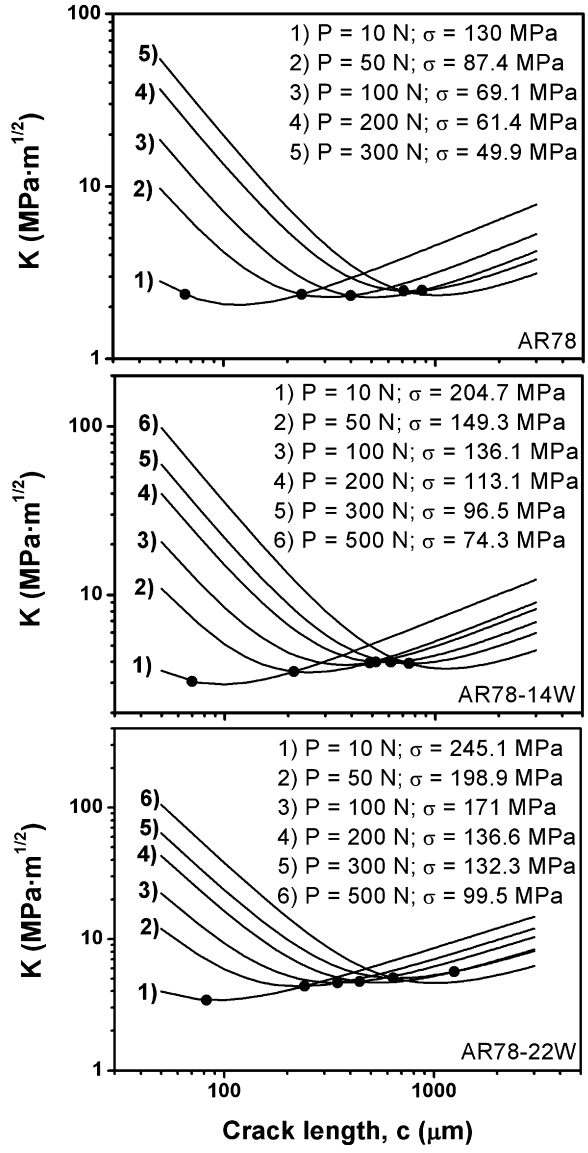

Fig. 4. R-curve diagrams for spinel and spinel/tungsten composites. Solid curves are plots of K_t vs. crack length from Eq. (1) at a particular indentation load and corresponding indentation strength indicated at the plot. The points define the locus of the R-curve and are calculated from Eq. (4).

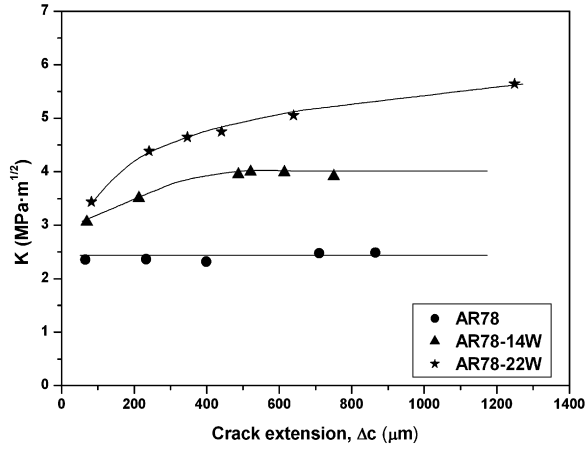

Fig. 5. Comparison of the R-curves measured in spinel and spinel/tungsten composites.

toughness (K_{ss}) is achieved at a crack length of ≈400 μm. On the other hand, in the case of monolithic spinel (AR78) such rising *R*-curve is not showed, as a consequence of its transgranular fracture mode that results in a lack of wake bridging, so a constant value of toughness is observed characteristic of brittle materials. These experimental results obtained with indentation strength test show that the spinel/tungsten composites develop "crack growth resistance".

The crack growth resistance, and therefore the flaw tolerance, in the case of AR78-22W composite are more important because the number of tungsten grains involved in the crack bridging is higher than in the 14 vol.% composite. After analyzing fracture surfaces for both composites (and in terms of comparison for the pure spinel) (Fig. 6), it is revealed that just larger (irregular) metal particles suffer plastic deformation (necking) when cracks make progress and interlock bridging is showed. On the other hand, smaller W particles (rounded and <2 μm) suffer intergranular fracture. The cracks advance along the metal/ceramic interface and pull out is observed. The increment in toughness value observed in these composites can be explained by the plastic deformation of the larger metallic particles (irregular shaped and >2 μm) in the crack bridging. Fig. 7 shows that, once the crack has reached the particle–matrix interface, the difference in the crack-tip opening displacement between the ductile particle and the brittle matrix will cause the crack to be locally blunted and its segments forced to circumvent the particle, thus bridging the crack along its length. This toughening mechanism requires both (i) strong metal–ceramic bonding and (ii) high plasticity of the metal particles.

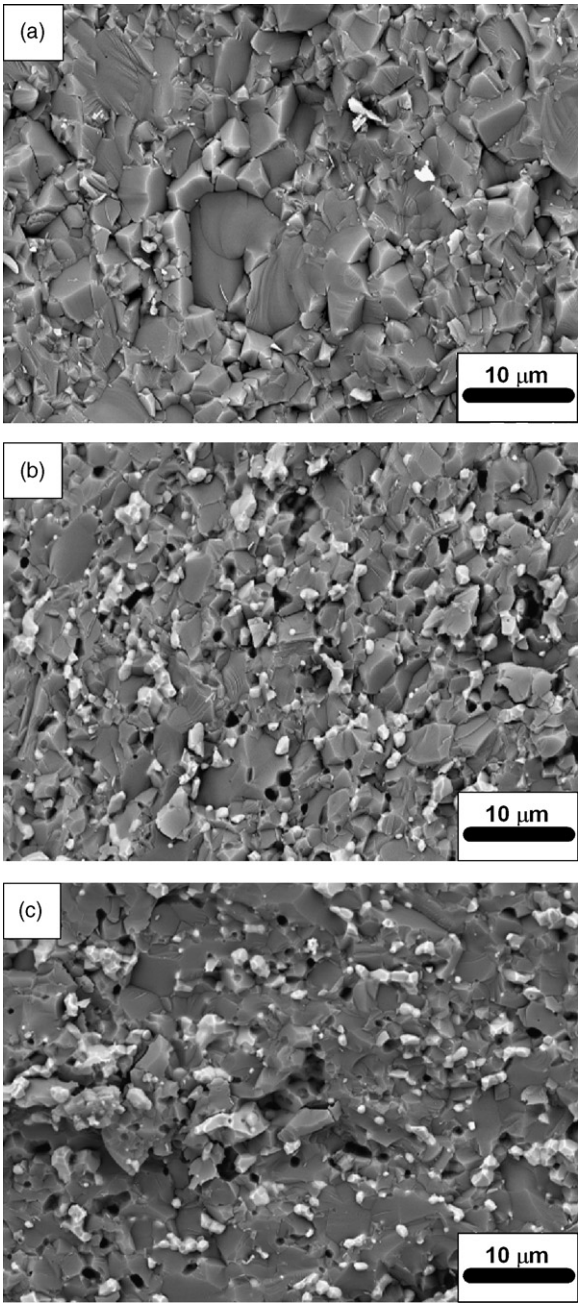

Fig. 6. SEM micrographs of fracture surfaces of (a) AR78; (b) AR78-14W; (c) AR78-22W composites.

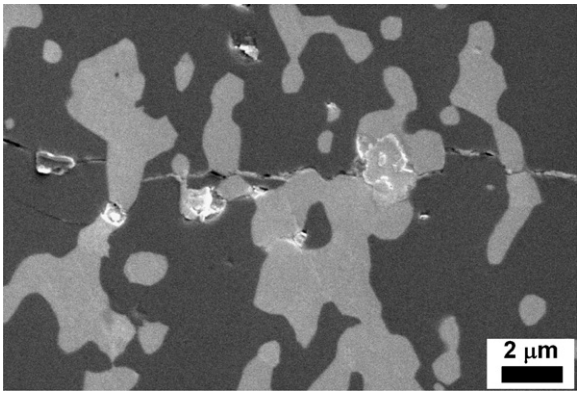

Fig. 7. Stretched W ligaments bridging the crack faces as observed on the crack profile of spinel/tungsten AR78-22W composite.

A similar behavior has been observed in mullite/molybdenum composites by Bartolomé et al.[17] It is explained that crack growth resistance is improved by increasing metal grain size and its volume fraction; this fact is also observed in spinel/tungsten composites. When metal content is higher, tungsten trends to agglomerate, thus metal grain size is larger and the amount of effective particles involved in bridging is higher as well as the toughening increases.

4. Conclusions

The following conclusions can be drawn:

(1) The spinel/tungsten composites exhibited progressively weaker sensitivity of strength to indentation load (flaw size) with increasing tungsten content in the composite; in other words, flaw tolerance improved with increasing metal content (related to larger metallic particles grain size and higher number of effective particles involved in toughening).
(2) The increase in the resistance of these ceramic–matrix composites with adherent ductile phase to crack propagation with crack extension (rising *R*-curve behavior) can be attributed to clamping forces applied by metal ligaments that bridge the crack faces behind the crack front. This metal

phase was shown to provide toughening by remaining intact behind a propagating crack front and applying closure forces that impeded crack growth.

(3) It has been demonstrated once again that one of the most important factors in the determination of fracture resistance are the metal phase dimension and shape. The smaller the metal phase, the smaller bridging area and the smaller fracture resistance. Coarse W particles enhanced the bridging effect, and as a consequence, a higher toughness value was achieved.

Acknowledgements

This research has been supported by the Spanish Ministry of Education and Science under the project MAT2003-04199-C02-01 and by the autonomous region of Madrid under project GR/MAT/0432/2004. S. Lopez-Esteban and J.F. Bartolomé have been supported by the Spanish Ministry of Education and Science under Ramón y Cajal Program.

References

1. Pyzick, A. J., Aksay, I. A. and Sarikaya, M., Microdesigning of ceramic–metal composites. In *Ceramic microstructure'86. Role of interfaces*, ed. J. A. Pask and A. G. Evans. Plenum Press, New York, 1987, pp. 45–54.
2. Sun, X. and Yeomans, J., Optimization of a ductile-particle-toughened ceramic. *J. Am. Ceram. Soc.*, 1996, **79**(10), 2705–2717.
3. Ung, T., Liz-Marzán, L. M. and Mulvaney, P., Optical properties of thin films of Au/SiO_2 particles. *J. Phys. Chem. B*, 2001, **105**, 3441–3452.
4. Gittleman, J. I., Goldstein, Y. and Bozozowski, S., Magnetic properties of granular nickel films. *J. Phys. Rev. B*, 1972, **5**, 3609.
5. Dericioglu, A. F. and Kagawa, Y., Effect of grain boundary microcracking on the light transmittance of sintered transparent $MgAl_2O_4$. *J. Eur. Ceram. Soc.*, 2003, **23**, 951–959.
6. Shimada, M., Endo, T., Saito, T. and Sato, T., Fabrication of transparent spinel polylycrystalline materials. *Mater. Lett.*, 1996, **28**, 413–415.
7. Wei, G. C., Transparent ceramic lamp envelope materials. *J. Phys. D: Appl. Phys.*, 2005, **38**, 3057–3065.
8. Guo, J., Lou, H., Zhao, H., Chai, D. and Zheng, X., Dry reforming of methane over nickel catalysts supported on magnesium aluminate spinels. *Appl. Catal. A: Gen.*, 2004, **273**, 75–82.
9. Guo, J., Lou, H., Zhao, H., Wang, X. and Zheng, X., Novel synthesis of high surface area $MgAl_2O_4$ spinel as catalyst support. *Mater. Lett.*, 2004, **58**, 1920–1923.
10. Beauvy, M., Dalmasso, C., Thiriet-Dodane, C., Simeone, D. and Gosset, D., Damages in ceramics for nuclear waste transmutation by irradiation with swift heavy ions. *Nucl. Instrum. Meth. Phys. Res. B*, 2006, **242**, 557–561.
11. Patterson, M. C. L., DiGiovanni, A. A., Roy, D. W. and Gilde, G., Spinel armor—clearly a way to go. *Ceram. Transact.*, 2003, **151**, 83–90.
12. Gusmano, G., Montesperelli, G., Traversa, E., Bearzotti, A., Petrocco, G., D'Amico, A. *et al.*, Magnesium aluminium spine1 thin film as a humidity sensor. *Sens. Actuators B*, 1992, **7**, 460–463.
13. Mukhopadhyay, S., Ghosh, S., Mahapatra, M. K., Mazumder, R., Barick, P., Gupta, S. *et al.*, Easy-to-use mullite and spinel sols as bonding agents in a high-alumina based ultra low cement castable. *Ceram. Int.*, 2002, **28**, 719–729.
14. Umemoto, A., Hayashi, K., Nakashima, K., Saito, N., Kaneko, K. and Ogi, K., High-intensity discharge lamp with Mo–SiO_2 functionally graded material. *J. Am. Ceram. Soc.*, 2006, **89**(3), 1133–1135.
15. Fleischer, N., Genut, M. and Gorodnev, A., Shock wave protection materials. *Am. Ceram. Soc. Bull.*, 2006, **85**(3), 27–28.
16. Speyer, R. F. and Judson, E. A., New process makes complex-shaped armor a reality. *Am. Ceram. Soc. Bull.*, 2006, **85**(3), 21–23.
17. Bartolomé, J. F., Díaz, M. and Moya, J. S., Influence of the metal particle size on the crack growth resistance in mullite–molybdenum composites. *J. Am. Ceram. Soc.*, 2002, **85**(11), 2778–2784.
18. Lopez-Esteban, S., Bartolomé, J. F., Pecharromán, C. and Moya, J. S., Zirconia/stainless-steel continuous functionally graded material. *J. Eur. Ceram. Soc.*, 2002, **22**(16), 2799–2804.
19. Lopez-Esteban, S., Bartolomé, J. F., Moya, J. S. and Tamimoto, T., Mechanical performance of 3Y-TZP/Ni composites: tensile, bending, and uniaxial fatigue tests. *J. Mater. Res.*, 2002, **17**, 1592–1600.
20. Braun, L. M., Benninson, S. J. and Lawn, B. R., Objective evaluation of short-crack toughness curve using indentation flaws: case study on alumina-based ceramics. *J. Am. Ceram. Soc.*, 1992, **75**(11), 3049–3057.
21. Raju, I. S. and Newman Jr., T. C., Stress-intensity factors for a wide range of semi-elliptical surface cracks in finite-thickness plates. *Eng. Fract. Mech.*, 1979, **II**, 817–829.
22. Anstis, G. R., Chankitul, P., Lawn, B. R. and Marshall, D. B., A critical evaluation of indentation techniques for measuring fractures toughness. I. *J. Am. Ceram. Soc.*, 1981, **64**(9), 533–538.
23. Hsueh, Ch.-H. and Becher, P. F., Determination of the *R*-curve from the strength indentation load relation. *J. Am. Ceram. Soc.*, 1995, **78**(8), 2237–2239.